remote sensing

MDPI

EO-1 data quality and sensor stability with changing orbital precession at the end of a 16 year mission

Shannon Franks[1,2],*, Christopher S.R. Neigh[1], Petya K. Campbell[1,3], Guoqing Sun[1,4], Tian Yao[1,5],

Qingyuan Zhang[1,5], Karl F. Huemmrich[1,3], Elizabeth M. Middleton[1] , Stephen G. Ungar[1,5] and

Stuart W. Frye[1,2]

[1] NASA's Goddard Space Flight Center, Code 618, Greenbelt, MD 20771, USA ;
    christopher.s.neigh@nasa.gov, elizabeth.m.middleton@nasa.gov
[2] Stinger Ghaffarian Technologies (SGT), Greenbelt, MD 20770, USA ; stuart.w.frye@nasa.gov
[3] University of Maryland, Baltimore County, Baltimore, MD 21250, USA ; petya.k.campbell@nasa.gov,
    karl.f.huemmrich@nasa.gov
[4] University of Maryland, College Park, College Park, MD 20740, USA ; guoqing.sun@nasa.gov
[5] Universities Space Research Association, Baltimore County, Columbia, MD 21044, USA;
    tianyao@hotmail.com, qingyuan.zhang@nasa.gov, stephen.g.ungar@nasa.gov

* Correspondence: shannon.franks@nasa.gov; Tel.: +01-301-614-6682

Abstract: The Earth Observing One (EO-1) satellite has completed 16 years of Earth observations in early 2017. What started as a technology mission to test various new advancements turned into a science and application mission that extended many years beyond the satellite's planned life expectancy.   EO-1's primary instruments are spectral imagers: Hyperion, the only civilian full spectrum spectrometer (430-2400 nm) in orbit; and the Advanced Land Imager (ALI), the prototype for Landsat-8's pushbroom imaging technology.   Both Hyperion and ALI instruments have continued to perform well, but in February 2011 the satellite ran out of the fuel necessary to maintain orbit, which initiated a change in precession rate that led to increasingly earlier equatorial crossing times during its last five years.   The change from EO-1's original orbit, when it was formation flying with Landsat-7 at a 10:01am equatorial overpass time, to earlier overpass times results in image acquisitions with increasing solar zenith angles (SZAs). In this study, we take several approaches to characterize data quality as SZAs increased. Our results show that for both EO-1 sensors, atmospherically corrected reflectance products are within 5 to 10% of mean pre-drift products. No marked trend in decreasing quality in ALI or Hyperion is apparent through 2016, and these data remain a high quality resource through the end of the mission.

1. Introduction

High quality data are of utmost importance for scientific studies and measurement stability over time is critical to evaluate seasonal, annual, and decadal changes [1]. In satellite remote sensing, analysts need to be sure that the imagery comes from well calibrated and characterized sources and the EO-1 satellite is no exception.

EO-1 was launched on November 21, 2000 as a one-year technology validation and demonstration mission. EO-1, at 572 kg total mass, approaches the smallest (< 500 kg) class of spacecraft. It was initially tasked with testing advancements that could potentially increase sensor performance while reducing instrument mass, power consumption, and cost. The three primary instruments on the EO-1 spacecraft were designed to acquire visible through near-infrared (VNIR)

and shortwave infrared (SWIR) wavelength information in the solar reflected spectrum [2]. These are the Advanced Land Imager (ALI), the Hyperion, and the Linear Etalon Imaging Spectrometer Array (LEISA) Atmospheric Corrector (LAC), which is not discussed further in this contribution.

EO-1 demonstrated that its 8-band multispectral (MS) imager, ALI, provides a significant improvement over the Landsat 7 Enhanced Thematic Mapper plus (ETM+) and previous Landsat Thematic Mapper (TM) instruments due to increased signal to noise ratio, while decreasing instrument size and weight. EO-1 also validated the scientific value of orbital imaging spectroscopy with Hyperion, the first spaceborne hyperspectral land imaging instrument. EO-1 also demonstrated that a moderate-spatial/high-spectral resolution imager could be used in self-correction of atmospheric effects to retrieve the apparent surface reflectance from top of atmosphere (TOA) radiances, and systematic errors [3]. It was originally thought that these new technologies could improve the TM/ETM+ sensor series found on the Landsat 4 - 7 satellites [4,5] and indeed, some of these technologies were utilized for the Landsat 8 Operational Land Imager (OLI) sensor launched in 2013, with, for example, the adoption of the push-broom style sensor and improved quantization [6,7].

With no indication of sensor degradation through the end of the one-year baseline mission in 2001, the EO-1 mission was extended, allowing ALI and Hyperion to continue collecting images [3]. The mission was chartered to collect and distribute ALI MS and Hyperion hyperspectral products in response to Data Acquisition Requests (DARs), which were soon established as a collaboration with the U.S. Geological Survey (USGS) Earth Resources Observation and Science (EROS) Data Center (EDC). There were four extensions of the mission [8], during which normal operations continued and the daytime imagery were used in numerous science investigations [9] ranging from characterizing forest structure [10-12], water quality [13,15] and desert dust flows [16], to disaster monitoring activities [17-19]. Additionally, the nighttime imagery was greatly utilized by the volcano monitoring network [20,21].

1.1. Orbital Precession Rate Change

From 2001 to 2007, EO-1 was flying in orbital formation with Landsat 7 (one minute behind). In late 2007 EO-1 began a de-orbit procedure, but barely a month into the process NASA gave EO-1 a re-entry waiver, and all remaining fuel was used to maintain the current orbit, which by then was slightly (~5 km) lower than Landsat 7. In 2011 EO-1 ran out of maneuvering fuel and the orbital degradation began, with a slowly changing rate of precession leading to increasingly earlier ground overpass times (Figure 1). A second waiver was issued for EO-1 to continue operations to study the effects of changes in precession on data quality.

In 2011, EO-1 lost its ability to maintain an exact sun synchronous precession orbit when the satellite depleted its onboard maneuvering fuel and could no longer make corrective "inclination burns". EO-1's orbital plane is still precessing, but not at the rate required to achieve precise Sun synchronicity, resulting in nadir observation times drifting towards earlier local overpass times. The implication for this is that specific targets are now viewed under different illumination conditions per month of the year, as compared to earlier phases of the mission (Figure 2).

Solar zenith angle (SZA) depends on local overpass time, latitude, and date. The earlier overpass times experienced in the last few years of the mission result in larger SZAs. However, these values of SZAs have already been experienced by EO-1 for imagery collected at different latitudes and seasons. As can be seen in Figure 3, approximately 60% of the time in 2016 the SZAs at EO-1 overpass times were within the previously experienced range of SZAs for that latitude.
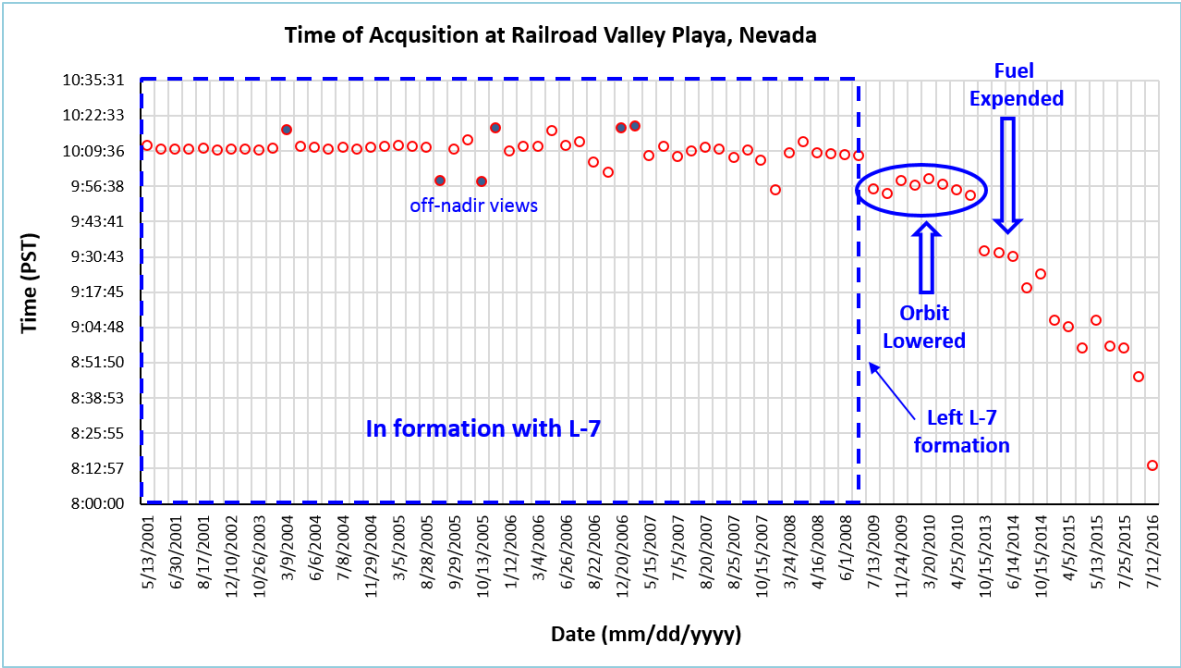
Figure 1. EO-1 changes in precession rate started in 2011. Acquisition time at the Railroad Valley Playa declined from 10:12 to 8:14, reaching 8 AM in October, 2016. The stability of the overpass time from 2001 to 2008 is shown (within dotted box), for nadir views (open circles) as well as off-nadir views (filled circles). A 15 minute change in overpass time is indicated within ellipse, after EO-1 left the Landsat-7 formation. The decline of overpass time is indicated by the downward arrow, after onboard fuel was expended.
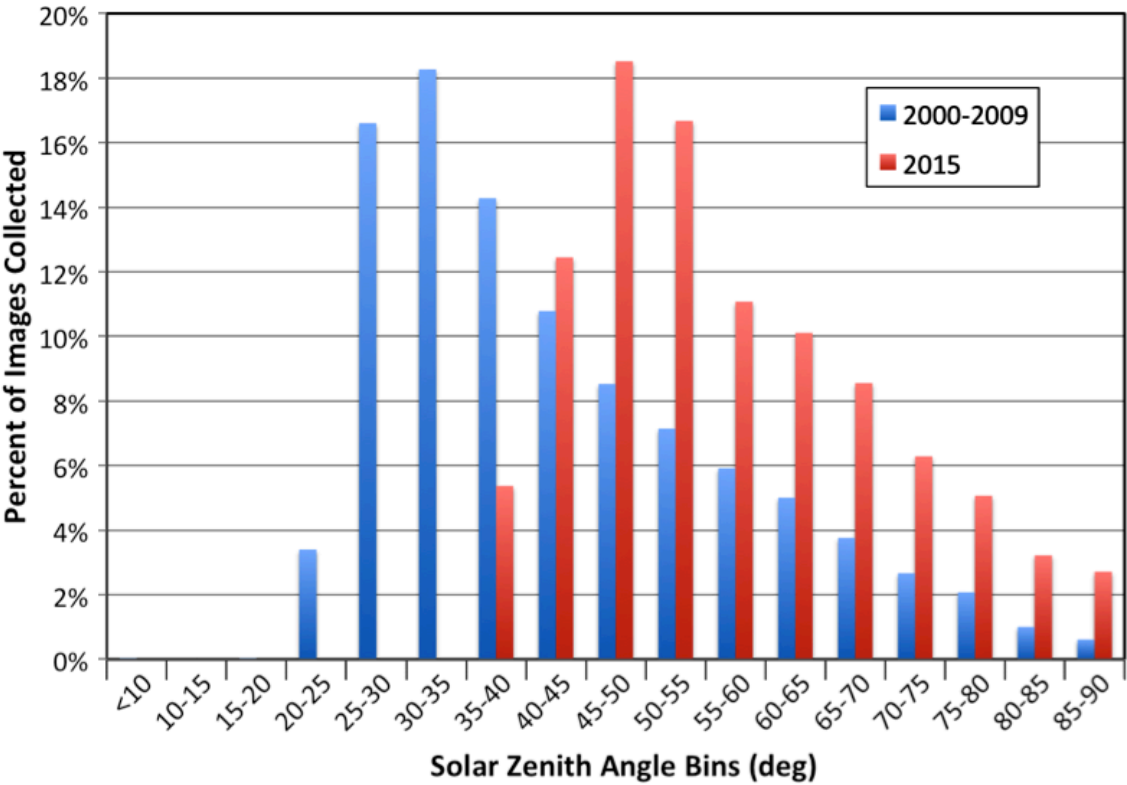

Figure 2. Solar zenith angles (SZAs), measured in degrees, of daytime Hyperion images. Due to the earlier acquisition times for the imagery, the distribution of SZAs at overpass times during 2015 shifted to larger values (red bars) than during the earlier normal mission operations (blue bars).
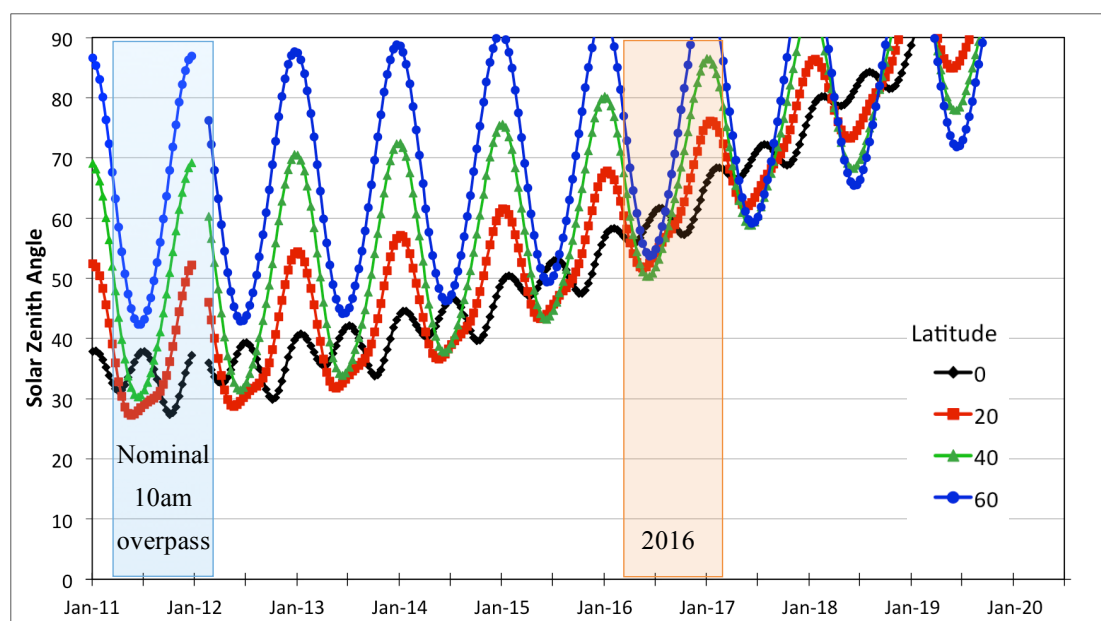
Figure 3. Solar Zenith Angles (SZAs) at EO-1 overpass time showing the effect of changing seasons and latitudes on SZAs as overpass time drifts to earlier times (colored lines, the colors indicating the latitude of the observation as shown in the legend). The blue shaded region shows SZAs at various latitudes during nominal operations, compared to SZAs experienced in 2016 (orange shaded region).

There are several potential impacts of changing orbital precession (also referred to as "drift" or "decay") [22]:

1. Larger SZAs due to the sun being closer to the horizon may reduce the quality of the signal by having weaker irradiances and a longer atmospheric path for radiances to traverse, which decreases the signal to noise (SNR) ratio of the data and complicates atmospheric correction procedures.

2. There is a change in the number of instances of cloudy data, which might be expected to increase in temperate zones as early morning haze is more often present and to decrease in tropical zones where convective clouds dominate [23].

3. The bi-directional reflectance distribution function (BRDF) of the data changes as the influence of shadows increases in concert with the illumination angles, and somewhat larger footprints are viewed. [24]

Understanding these effects of changing overpass times helps future mission planners to evaluate overpass times for sun synchronous missions as well as understanding the issues involved with integrating data from multiple satellites with different overpass times as proposed in future actual and virtual constellations. EO-1 became a natural experiment in this problem providing unique opportunities to evaluate these questions due to its long time series to which comparisons can be made.

Here, we examine quality and stability of the daytime imagery acquired by two EO-1 sensors to determine the effect of orbital precession on data products with changing SZAs and footprints in areas with different surface characteristics. We used multiple approaches in several locations with varying surface properties to highlight different aspects of the effects of EO-1's changing precession over time. We selected three vegetation sites and two Committee on Earth Observing Satellites (CEOS) Pseudo Invariant Calibration Sites (PICS) to evaluate data quality and stability changes.

2. Data and Methods

2.1 EO-1 Instrument Characteristics

134 The EO-1 ALI is an 8-band MS imager having a 15° Wide Field Telescope (WFT) and a partially
135 populated focal plane occupying 1/5th of the field-of-view, giving a ground swath width of 37 km.
136 Hyperion is a grating imaging spectrometer with a 7.7 kilometer swath and it provides 220
137 functional bands with an approximately 10 nm sampling interval from 430-2400 nm [3]. Both ALI
138 and Hyperion have 30 m nadir ground pixels to match Landsat-7. All collected data are archived
139 and distributed by the USGS/EROS data center [25].

140 *2.2 Study Methods*

141 Five different study sites were selected to evaluate the impacts of precession on surface
142 reflectance from Hyperion and ALI at different latitudes and land cover types to characterize sensor
143 performance (Table 1). It would have been desirable to have more test sites in differing regions of
144 the world, but it was difficult to find time series data, which was needed to show effects of
145 changing precession over time. This was because EO-1 was never conceptualized to be a robust
146 repeat sensor. For this reason, several of our selected sites were PIC sites.

147
148 1) Park Falls, Wisconsin: The Normalized Difference Vegetation Index (NDVI) [26,27]
149 obtained from ALI TOA reflectance was compared with that from Landsat NDVI, and
150 an NDVI difference was computed for a mixed forest site in multiple years;
151 2) Howland Forest, Maine: The NDVI obtained from Hyperion surface reflectance was
152 compared to the NDVI obtained with the Moderate Resolution Imaging
153 Spectroradiometer (MODIS) for an experimental mixed forest, in multiple years;
154 3) U.S. Department of Agriculture/Beltsville Agriculture Research Center (USDA/BARC)
155 in Beltsville, Maryland: The temporal change in the Hyperion surface reflectance was
156 evaluated using 1st derivative analysis, in an agriculture site over multiple years;
157 4) Rail Road Valley Playa (RRVP), Nevada: For a Pseudo-Invariant Calibration Site (PICS),
158 a Hyperion surface reflectance time-series was evaluated for a bright desert target site;
159 and
160 5) The Libya-4 PICS, Libya: Statistical evaluation of the change in surface reflectance
161 obtained in different spectral intervals and over time was evaluated using a dense
162 Hyperion surface reflectance time-series for a bright desert target site.

163 **Table 1.** Dominant land cover types and Northern Hemisphere study site locations used in
164 analyses

Site Name	Central Coordinates (longitude, latitude)	Dominant Land Cover
Park Falls, Wisconsin	90.18° W, 45.58° N	Mixed hardwood forest
Howland Forest, Maine	68.5° W ,45.21° N	Mixed coniferous forest
BARC[1], Maryland	76.85° W, 39.03° N	Evergreen, Corn Field
RRVP[2], Nevada PICS	115.69° W, 38.5° N	Desert
Libya- 4 PICS[3]	24.40° E, 28.53° N	Desert

[1] Beltsville Agricultural Research Center, [2] Rail Road Valley Playa, [3] Pseudo-Invariant Calibration Site

165 2.2.1. Park Falls Wisconsin – EO-1/ALI NDVI vs. Landsat NDVI

166 Park Falls, Wisconsin was chosen as the study site for this experiment because of the density of
167 EO-1 imagery available and the diversity of included land cover types. This site falls within the
168 Worldwide Reference System (WRS) path 25, row 28. One ALI image per year from summers of
169 2001 to 2016 were selected and a corresponding Landsat image was chosen to minimize the
170 difference between the dates of acquisition (Table 2). For the twelve pairs of images, the cumulative
171 delta days between all acquisitions were 19 days, averaging just 1.58 days/pair. Comparison of the
172 spectral bandwidths (Table 3) of each sensor shows that all bands except the Near Infrared (NIR)
173 have very similar wavelength ranges. Sun and view angle differences also play a part in NDVI

174 calculation [28]. Solar zenith angle differences were minimalized as acquisitions of the comparitive
175 scenes were all within a few days of one another so solar zenith angles were all very close. When
176 considering view angles, Landsat images are always nadir viewing whereas EO-1 has the ability to
177 view up to one neighboring WRS path on each side. With this in mind, the EO-1 images were
178 selected to reduce impacts of view angle and all but one had view angles less than 7.5 degrees. The
179 2016 ALI image had an off-nadir angle of 20 degrees, but it has been demonstrated that NDVI is not
180 highly effected until this angle is greater than 25 [28].

181

Table 2. Coupled image pairs used for the Park Falls, WI analysis.

Landsat date	ALI date	Off nadir
8/17/2016	8/17/2016	20.10
8/15/2015	8/13/2015	-0.30
8/12/2014	8/09/2014	-5.70
9/26/2013	9/27/2013	6.10
8/06/2012	8/05/2012	4.50
8/20/2011	8/27/2011	-2.72
8/17/2010	8/17/2010	-2.50
9/23/2009	9/21/2009	-1.00
9/12/2008	9/09/2008	5.60
6/30/2007	6/30/2007	-7.20
8/11/2002	8/11/2002	3.50
5/04/2001	5/04/2001	0.13

182

Table 3. Wavelengths ranges per band for each ALI, TM, and ETM+ sensor

	EO-1 ALI	Landsat 5	Landsat 7
	Wavelength (μm)	Wavelength (μm)	Wavelength (μm)
Pan [1]	0.48 - 0.69		.52-.90
Blue'	0.43 - 0.45		
Blue	0.45 - 0.52	0.45-0.52	0.45-0.52
Green	0.53 - 0.61	0.52-0.60	0.52-0.60
Red	0.63 - 0.69	0.63-0.69	0.63-0.69
NIR	0.78 - 0.81	0.76-0.90	0.77-0.90
NIR'	0.85 - 0.89		
SWIR'	1.20 - 1.30		
SWIR 1	1.55 - 1.75	1.55-1.75	1.55-1.75
TIR		10.40-12.50	10.40-12.50
SWIR 2	2.08 - 2.35	2.08-2.35	2.09-2.35

183 [1] Pan = Pancromatic

184 Data for the EO-1 and Landsat sensors were downloaded from USGS in units of TOA
185 reflectance and had radiometric and systematic geometric corrections applied to achieve a Level
186 One Terrain corrected and ortho-rectified (L1T) image product. An NDVI product was obtained
187 from ALI and Landsat scenes, as a normalized difference spectral index using Equation (1) [27]:

$$NDVI = \frac{\rho_{NIR} - \rho_{red}}{\rho_{NIR} + \rho_{red}} \tag{1}$$

188 Each Landsat image was subset to the boundaries of the EO-1 ALI imagery to have exactly the
189 same region of interest for statistical calculations. A data cube was built with these stacked
190 images. To establish land cover classes, the 2011 National Land Cover Database (NLCD) [29] was
191 downloaded and overlayed onto the data stacks.
192 For the analysis, the NDVI associated with each pixel was differenced (ALI minus Landsat)
193 and those differences were averaged per NLCD land cover class. In our experience from visually
194 looking at pixels with large NDVI differences, any delta NDVI between the ALI and Landsat data
195 greater than 0.15 were most likely due to something other than sensor difference. These other
196 differences could be from clouds, a rain event, or a land disturbance in one of the images, and we
197 removed them from the comparison.

198 2.2.2. Howland Forest, Maine – Hyperion NDVI comparison to MODIS NDVI

199 Three Aflux tower sites (US-Ho1: 45.20° N, -68.74° W; US-Ho2: 45.21° N, -68.74° W; and
200 US-Ho3: 45.21° N, -68.73° W) in the Howland Experimental Forest, Maine were chosen for the
201 analysis of Hyperion NDVI vs. MODIS NDVI, utilizing imagery collected between 2003 and 2014,
202 with representation from all seasons. All three sites were mixed evergreen forest with a warm
203 summer climate and significant precipitation in all seasons. The mean average temperatures are
204 slightly over 5°C and the elevation ranged from 60 to 90m. The spatial resolution of nadir MODIS
205 data is either 500 m or 1 km, while the spatial resolution of Hyperion data is 30 m. Thus, the
206 reflectance values of Hyperion data have been aggregated spatially to match MODIS pixels at either
207 500 m or 1 km resolution. To see phenology variability using the EO-1/Hyperion reflectance data
208 product, the Hyperion NDVI data were compared with NDVI derived from MODIS by differencing
209 the spectral pixel values.
210 The Hyperion Level 1 GST (L1GST) product having radiometric and geometric corrections as
211 well as a systematic terrain correction were downloaded and used for this analysis. The Hyperion
212 L1GST images were atmospherically corrected using the Atmosphere Removal Algorithm
213 (ATREM) [30] [31]. Hyperion NDVI data (using Eqn. 1) were calculated from the surface reflectance
214 using bands 27 – 32 and 49 - 54 of the L1GST product. The NDVI data from the MODIS satellite
215 instrument were calculated from surface reflectance in MODIS bands 1 (620 – 670 nm) and band 2
216 (841 – 876 nm). MODIS Level 1B calibrated radiance data (MOD021KM and MOD02HKM) and
217 geolocation data (MOD03) were downloaded from the NASA Level-1 and Atmosphere Archive &
218 Distribution System (LAADS) [32] website. A modified gridding approach was used in this study,
219 where the flux tower was located in the center of related 500 m or 1 km grids [33]. MODIS L1B
220 radiance data from each swath were then gridded at 500 m or 1 km resolution for MODIS bands 1–2
221 with appropriate area weights of each MODIS observation. MODIS data were processed by the
222 modified gridding method and the gridded observations were atmospherically corrected by the
223 Multi-Angle Implementation of Atmospheric Correction (MAIAC) algorithm [34].

224 2.2.3. BARC – Surface reflectance at USDA site with derivative analysis

225 To study the stability of reflectance for differing types of vegetation targets, Hyperion data
226 acquired for the USDA BARC in Maryland were collected and used. The Hyperion Level 1T data
227 were acquired in the summer and fall from 2005 – 2015 and calibrated to surface reflectance by the
228 Fast Line-of-sight Atmospheric Analysis of Spectral Hypercubes (FLAASH) software [35] using
229 default model parameters for typical summer/fall clear-sky atmospheric conditions. The acquisition
230 time, sensor look angle, center location of the data and a visibility of 40 km were used as inputs for
231 MODerate resolution atmospheric TRANsmission (MODTRAN) parameters.
232 Derivative analysis is a powerful tool that enhances the interpretation of data. Derivatives of
233 second order or higher should be relatively insensitive to variations in illumination intensity

234 whether caused by changes in sun angle, cloud cover, or topography [36]. Kalluri et al. [37] used
235 spectral derivatives and single or multiple classifiers in land classification and achieved overall
236 classification accuracy (expressed in percentage) that was significantly greater than was achieved
237 when exploiting only the reflectance information. In a study by Ye et al. [38], the classification
238 results in the spectral as well as derivative domains were fused by a logarithmic-opinion-pool rule
239 and the results demonstrated that the algorithms improved classification accuracy even in cases
240 with small   training sample sizes. When combined with time-series analysis, derivative analysis
241 reveals whether the signal is consistent, regardless of seasonal factors.
242   Derivatives are very sensitive to noise, so smoothing or minimizing random noise is important.
243 Tsai and Philpot [36] examined several methods for smoothing of hyperspectral data. In this study
244 the local polynomial regression fitting [39] was used to smooth the reflectance data before
245 derivatives were calculated.   1st, 2nd, and 3rd derivatives were calculated on the Hyperion spectra
246 (Equation 2), considering the full width at half maximum (FWHM) value of each wavelength
247 interval.

$$\frac{\Delta r_i}{\Delta \lambda} = \frac{r_i - r_{i-1}}{(FWHM)_i} \qquad (2)$$

248   Where $\Delta r_i / \Delta \lambda$ is the derivative and Δr_i is the change in reflectance, $\Delta \lambda$ is the change
249   of wavelengths, and FWHM is the full width at half maximum for that wavelength
250
251   Various targets (each having 10 to 30 pixels) were identified from Hyperion data using the
252 Region of Interest (ROI) tool of ENVI [40]. The mean reflectance of the targets were calculated for
253 152 calibrated bands of the Hyperion data. The calibrated bands consists of 5 pieces: 427 nm – 925
254 nm; 973 nm – 1114 nm; 1175 nm – 1326 nm; 1497 nm – 1790 nm and 2032 nm – 2355 nm. The width
255 for the local filtering was 30 nm.

256 2.2.4. Rail Road Valley Playa (RRVP) PICS – Surface Reflectance at a desert site

257   RRVP is among the PICSs endorsed by the Committee on Earth Observing Satellites (CEOS) to
258 serve as a standard reference for the post-launch calibration of space-based optical imaging sensors
259 [41]. RRVP is located in a large, dry lakebed in central Nevada and has a dry climate, typical of the
260 high desert of the western USA [42]. The site is characterized by high reflectance, relatively high
261 spatial and temporal uniformity, high midday sun elevation, and minimal cloud cover. The surface
262 layers and composition are relatively smooth and spatially homogeneous, consisting of compacted
263 clay-rich lacustrine deposits [43]. More description of the site and detailed spectral evaluations are
264 available in Scott et al. [42], Teillet et al. [43], and Czapla-Myers et al. [44,45]. Because of its large
265 size, RRVP is used for sensors with larger footprints (1–10 km), and is automated with
266 instrumentation used extensively for the vicarious calibration of terrestrial imaging sensors
267 covering the VNIR and SWIR wavelength ranges [44,45].
268   The Hyperion time series collection at RRVP was processed following the procedures outlined
269 in Campbell et al. [46]. Hyperion TOA radiances were converted to surface reflectance using the
270 Atmospheric CORrection Now (ACORN) software [47] and the module designed for pushbroom
271 imaging spectrometers with cross-track spectral calibration variation. According to the date of
272 acquisition, apparent surface reflectance was derived using either mid-latitude summer or winter
273 atmospheric models. To preserve the original spectral properties and variability, the images were
274 not geographically or geometrically rectified.   This was valid as a prior study established that at
275 RRVP, Moran I statistics vary between 0.81 and 0.95 across Hyperion's spectral range (1 = strong
276 positive spatial autocorrelation, 0 = spatially uncorrelated data), which was attributed to variation
277 in soil moisture affects and differences in the mineral composition of the surface [46]. We used band
278 subsetting to remove uncalibrated and overlapping bands, and bands adjacent to water absorption
279 features, resulting in subsets having 171 bands (Table 4).
280   Time series of Hyperion data were used to determine spectral stability during the period
281 previous to the precession change beginning in 2011 or during the changing satellite precession.

282 Thirty-seven radiometrically corrected Level 1R images from 2001 – 2015 were converted to surface
283 reflectance using the ACORN software. Mean reflectance and standard deviation (SD) were
284 calculated for select wavelength bands (Figure 4). These wavelengths were chosen as representative
285 of the spectral properties throughout the VNIR and SWIR wavelengths for RRVP. The mean was
286 calculated with data from 2001 – 2008. Twenty-three pre-precessional and fourteen
287 post-precessional images (see Figure 1 for dates) were used for the statistics of the change as delta
288 reflectance (Δp).

289

Table 4. Subset of bands used in RRVP study

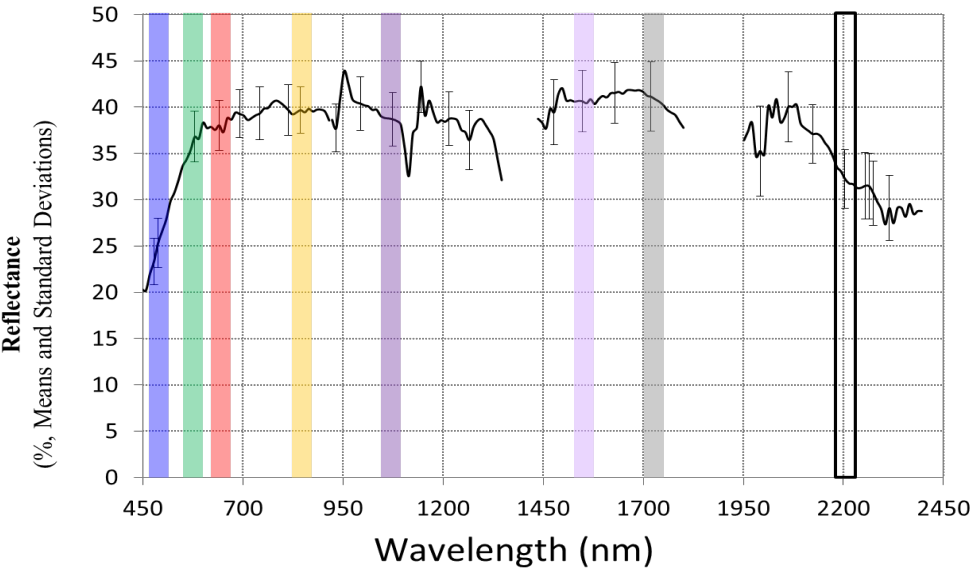| Array	Bands	Wavelengths (nm)
VNIR	8 - 57 (49)	426 - 926
SWIR1	7 - 120 (41)	993 - 1346
SWIR2	129 - 165 (36)	1518 - 1800
SWIR3	179 - 224 (5)	1942 - 2395
Total	(171)	

290

291

292 **Figure 4.** Mean reflectance and standard deviation for select wavelengths for the Rail Road Valley
293 Playa (RRVP) site before late mission precession changes (2001-2008 data, n=15 images, ~10:05 am
294 mean local time acquisition).

295 *2.2.5. Libya-4 PICS – Hyperion time-series using different atmopheric correction models*

296 To test differences of various atmospheric correction techniques and potential impacts of using
297 Hyperion for cross calibration, we used a time-series of surface reflectance data from 2004 — 2016
298 in the Libya-4 desert PIC site, which is commonly used as a calibration site for Earth observing
299 sensors.
300 Thirty-six images from WRS path 181, row 40 were co-registered. All data were nadir ±10 degrees
301 and collected between May and September to reduce seasonal SZA effects. These data were
302 atmospherically corrected to surface reflectance using ATREM, ACORN, and FLAASH [31,35,48].
303 ATREM uses a radiation transport model based on 6S, whereas ACORN and FLAASH use a more
304 complex radiation transport model that retrieves atmospheric properties from bands near
305 absorption features [49,50]. All three models account for differences in the measured upwelling
306 radiance from differences in solar irradiance due to different acquisition dates and times, and all
307 models had similar parameters applied for the Libya-4 PICS. Combined atmospheric model

308 uncertainty was estimated using a quadrature statistic [51], expressed as the square root of the
309 coefficient of variation of the sum of squares from each atmospheric correction approach.
310 A digital terrain model was also generated for this site using same date cross-track 50cm
311 panchromatic WorldView-1 and WorldView-2 stereo imagery to characterize terrain slope impacts
312 to reflectance products. Greater than 50 tie points were used and the RMSE for the product was less
313 than 3.5m with a resulting resolution of 2m. This was done because we wanted to see if SZA change
314 from precession combined with large dune shadowing at the site effected the results. More
315 information about how these data were processed is available in [52].

316 **3. Results**

317 *3.1. Park Falls, Wisconsin: EO-1 ALI NDVI vs. Landsat NDVI*

318 ALI analysis was comprised of two parts.   First, we wanted to know the spectral difference
319 between the calculated NDVI from the two sensors over the time series.   In the comparison of
320 NDVI from ALI and Landsat, the stratified images by cover type using the NLCD, only the low
321 intensity development class (class 22) showed much variance, which had larger NDVI differences
322 (between 0.05 and 0.10 Δ NDVI) than the others (see Figure 5). This difference may be attributed to
323 a smaller sample size compared to the other land cover classes. Second, we wanted to identify
324 changes in median ΔNDVI over time that occurred, possibly showing the manifestation of
325 increasing differences in SZA due to orbital drift of EO-1.   However, we show that there was no
326 systematic trend in ΔNDVI occurring since the onset of precession. In Fig. 5 for all classes, the
327 median difference hovers above and below zero with no observable trend. We hypothesized that if
328 precession was affecting ALI data quality that the differences would increase in either a positive or
329 negative fashion over time. Not including the low intensity development class (class 22), the highest
330 deviation was 0.05 NDVI, found in several classes and years, but all before precession started in
331 2011.

332 *3.2. Howland Forest, Maine – Hyperion NDVI comparison to MODIS NDVI*

333 Phenological changes in NDVI were compared between EO-1 Hyperion and MODIS surface
334 reflectances at three flux tower sites (US-Ho1, US-Ho2 and US-Ho3) in the Howland Experimental
335 Forest, Maine. NDVI maps were derived from EO-1 Hyperion images over the 6 km area
336 surrounding the three Howland Forest flux tower sites across four seasons from spring (March 5,
337 2014), summer (Aug. 12, 2014), fall (Sept. 22, 2008) and winter (Dec. 9, 2010). Figure 6 shows the
338 expected NDVI seasonality, with both the early and late year observations of low NDVI and high
339 mid-season NDVI responding to the presence of green leaves and higher photosynthesis.
340 For the areas around the three flux tower sites, NDVI was differenced between Hyperion
341 and MODIS data (Figure 6, lower plot). Similar to other results, the NDVI difference is small (i.e.
342 ΔNDVI < 0.15) and does not increase over time although it varies across years. Most of the large
343 NDVI differences (from 0.10 - 0.15) occur in US-Ho3 site (East Tower, Harvest Site), which is not as
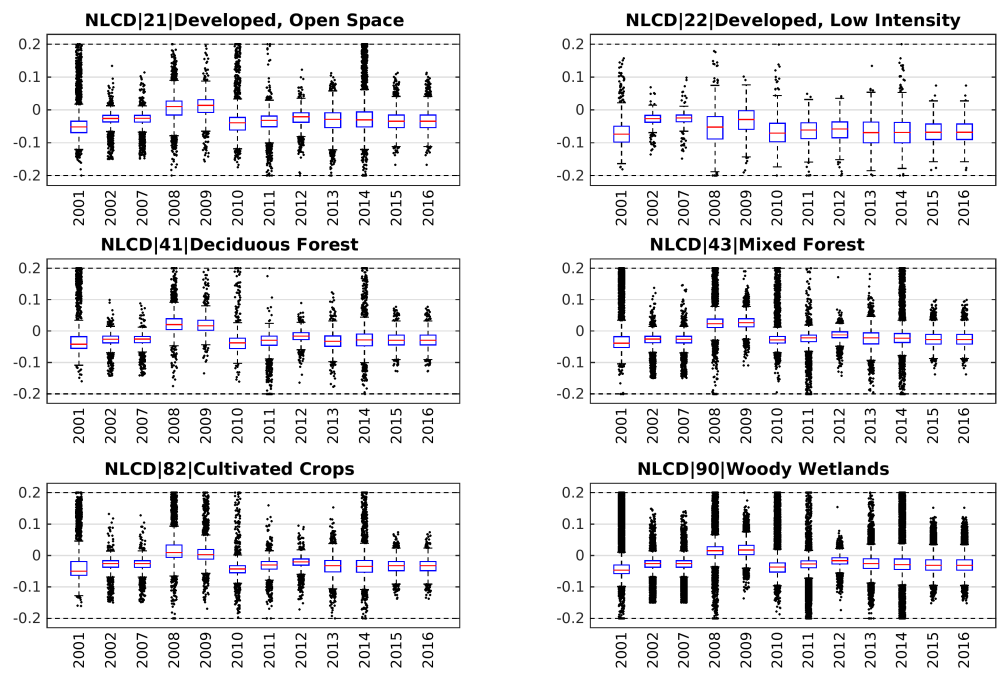344 homogeneous as the other two flux tower sites.
345

Figure 5. Statistics for median NDVI difference between Landsat and ALI sensors, per six National Land Cover Database (NLCD) classes. Red line is median, blue box is quartiles, and black crosses are outliers. NDVI values were derived from Top of Atmosphere (TOA) reflectance.
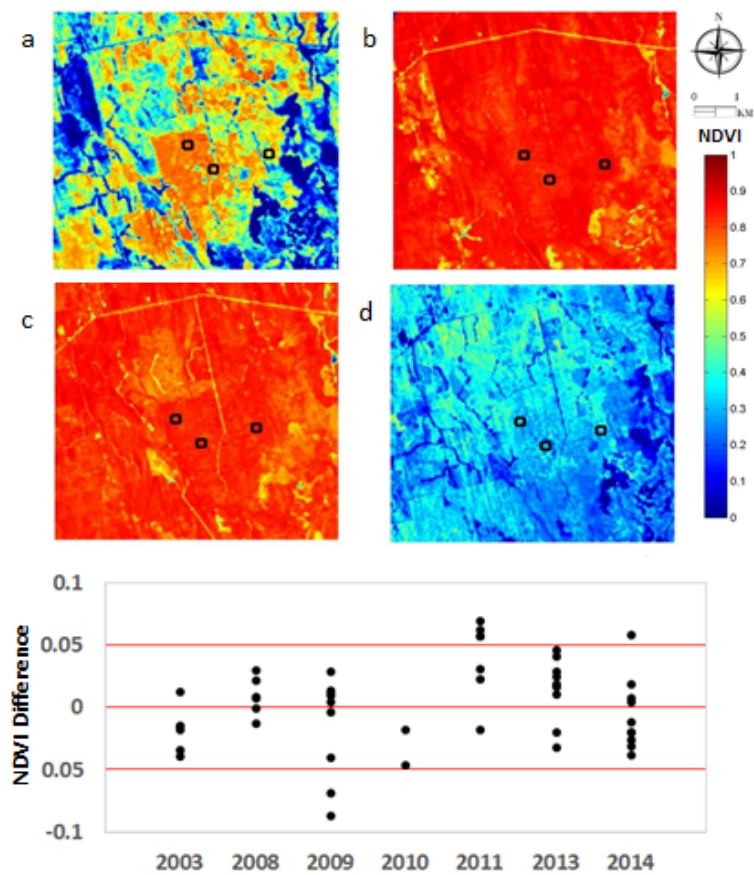

Figure 6. Upper chart: NDVI maps from EO-1 Hyperion images over the Howland Forest area in Maine across four seasons from: a) Spring; b) Summer; c) Fall; d) Winter. Three flux tower sites are

353   indicated with black squares.   Lower graph: NDVI difference between Hyperion and MODIS for
354   the three flux tower sites in the Howland forest area of Maine from 2003 to 2014.

355 *3.3. BARC – Hyperion surface reflectance derivative analysis*

356   At this USDA site, we chose targets with varying degrees of seasonal differences to determine
357 if derivative analysis displays a consistent signal throughout the Hyperion time-series. The spectral
358 reflectance and derivatives from four targets (corn field, evergreen trees, deciduous trees, and top
359 of building) are shown in Figure 7 & 8. As can be seen in the figures, the corn field has a very
360 different spectral reflectance between the five dates due to the differences in planting and
361 harvesting schedules in those years. The Evergreen patch and the top of a building, not
362 surprisingly, have a much more uniform reflectance among dates. The derivatives show the
363 consistency between different dates for a target and keep different features for different targets.

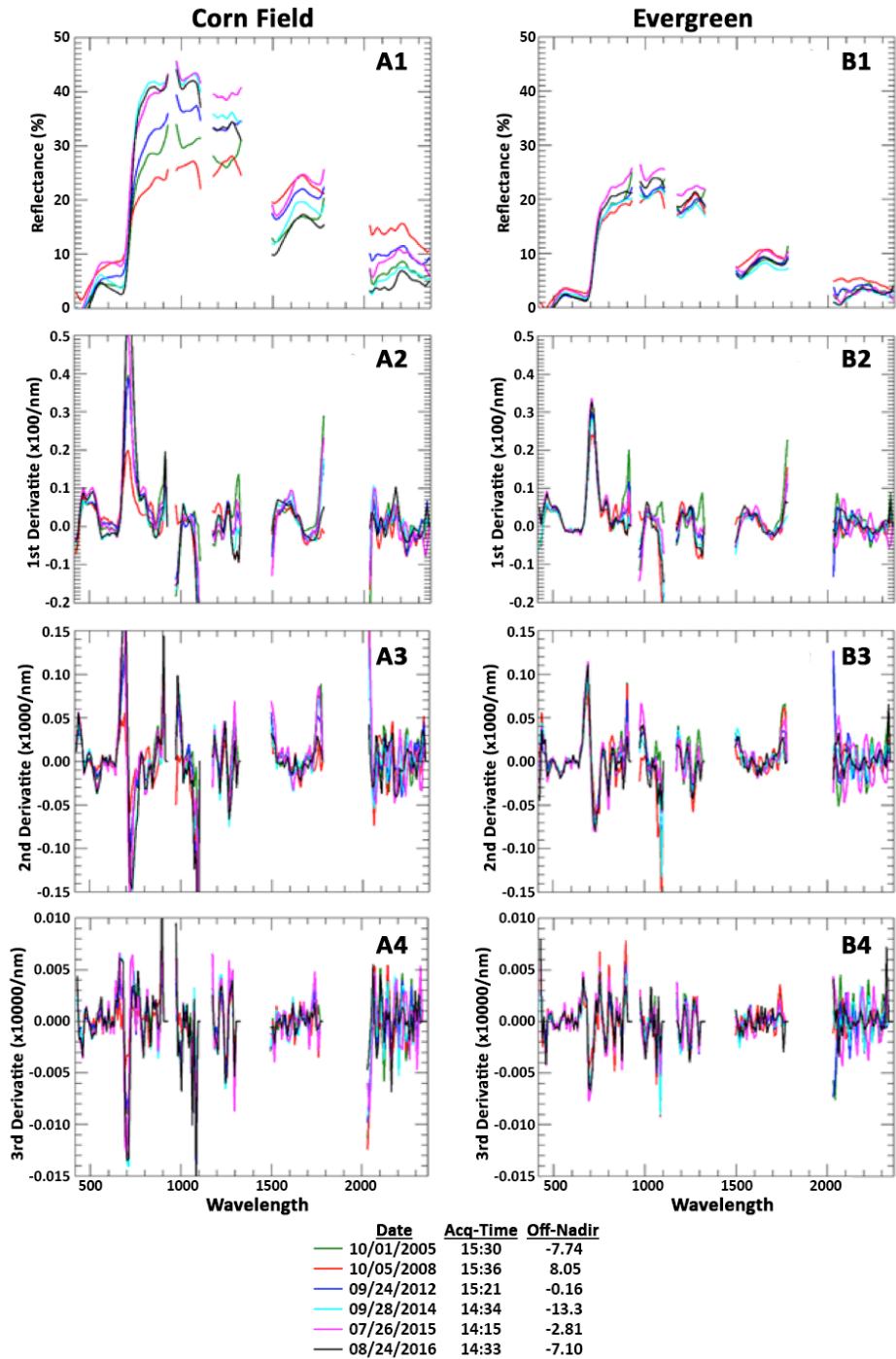| Date	Acq-Time	Off-Nadir
10/01/2005	15:30	-7.74
10/05/2008	15:36	8.05
09/24/2012	15:21	-0.16
09/28/2014	14:34	-13.3
07/26/2015	14:15	-2.81
08/24/2016	14:33	-7.10

364

Figure 7. Spectrum (top row) and 1st, 2nd, 3rd derivatives (rows 2 to 4) of a Corn field (column A) and Evergreen patch (column B).

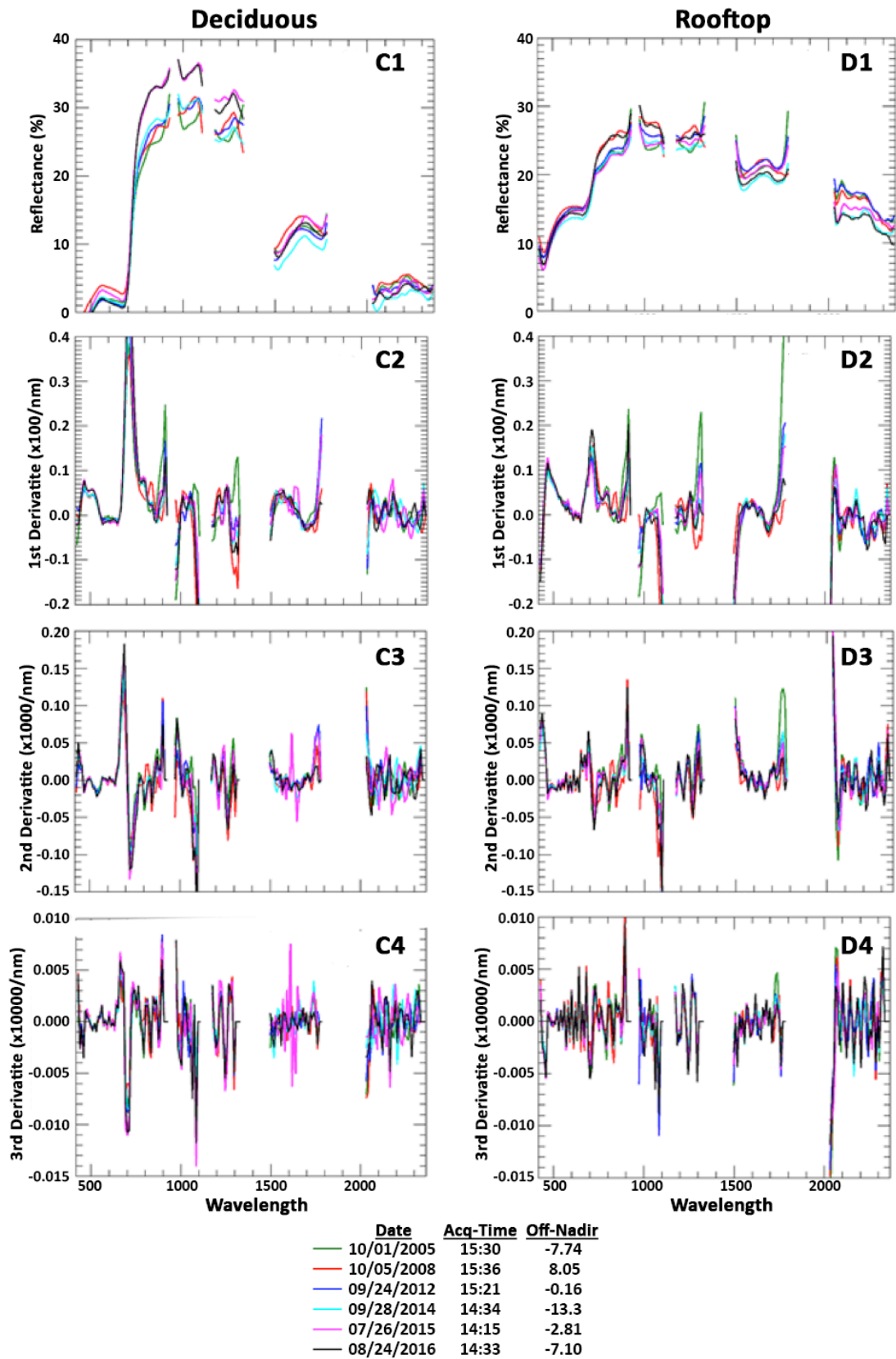| Date	Acq-Time	Off-Nadir
10/01/2005	15:30	-7.74
10/05/2008	15:36	8.05
09/24/2012	15:21	-0.16
09/28/2014	14:34	-13.3
07/26/2015	14:15	-2.81
08/24/2016	14:33	-7.10

Figure 8. Spectrum (top row) and 1st, 2nd, 3rd derivatives (rows 2 to 4) of a deciduous patch (column C) and Rooftop (column D).

370

371   *3.4. RRVP – Desert site surface reflectance time series*

372   Similar to the ALI NDVI vs. Landsat NDVI study above, we wanted to look at deviations in
373   reflectance of Hyperion data over time for a site with stable reflectance. Pre-precession means were
374   calculated and differenced from subsequent years of acquisitions over the same target and
375   wavelengths (Equation 3).   In the first few years of precession, reflectance values are lower than
376   pre-precession (Figure 9). From 2014 to early-2015 the values fluctuate about the mean and then
377   from early-2015 Hyperion reflectance values increase to stay consistently above the pre-precession
378   mean. However, the difference in reflectance continues to be within ± 5 - 9% of the mean prior to Δ
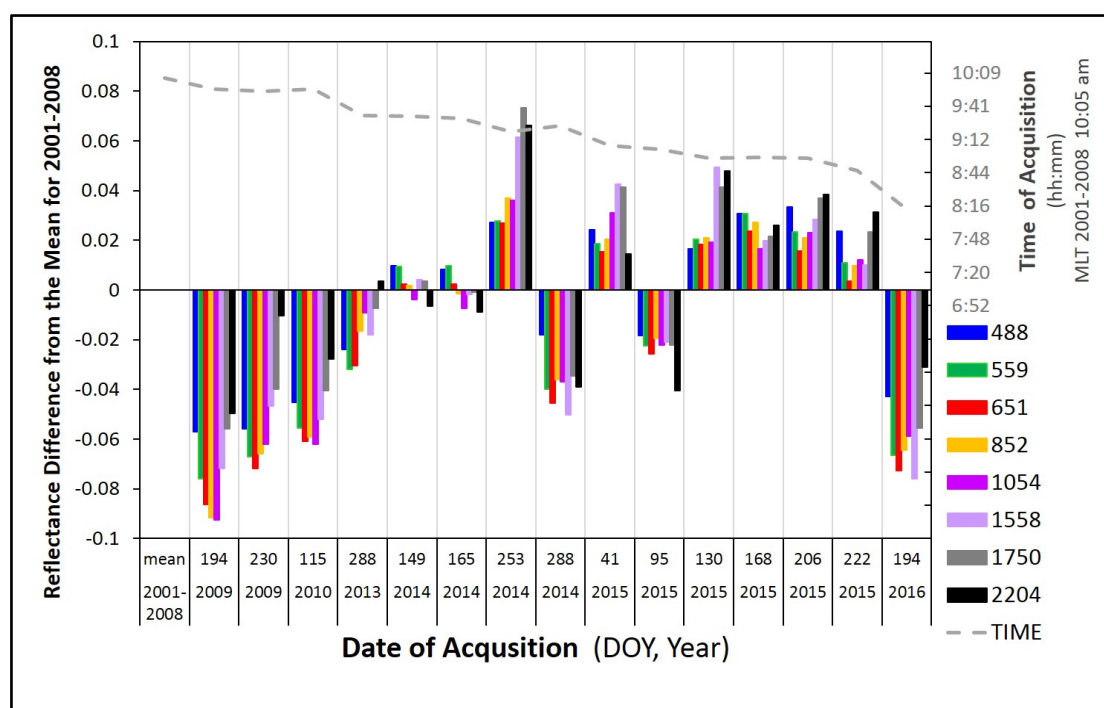379   precession. The regions of highest spectral stability (e.g, green, red edge, NIR) remain the same.

380

381   **Figure 9.**   Change in reflectance anomaly (Δp) at select wavelengths.   A mean was established by
382   averaging values from 2001-2008.   The dashed line above the bars shows the time of acquisitions
383   and the key for wavelengths is presented in the lower right legend.

$$(R_i = R_{mean\ 2001\text{-}2008} - R_{DOY,\ 2009\text{-}2015}),$$

Where R_i is the differenced reflectance, R_{mean} is the calculated mean,   (3)
and R_{DOY} is the reflectance per each observation after 2008.

384   *3.5. Libya-4 PICS – Hyperion surface reflectance stability using three atmopheric correction models*

385   We studied Hyperion precession from 2004 through 2016 with three atmospheric correction
386   algorithms to characterize temporal stability of surface reflectance products and to understand
387   uncertainties introduced by terrain shadow in the Libya-PICS. Hyperion data were stable in most
388   bands over this time period, independent of the atmospheric correction model used. However, the
389   imagery degraded at different rates throughout the spectrum for the visible (VIS), NIR, infrared
390   (IR), and SWIR between 2004 to 2016, as indicated through the several atmospheric correction
391   techniques. The combined model variation expressed as a quadrature was within 10% for the VNIR
392   and in most SWIR bands the variability was within 20%, excluding bands near atmospheric
393   absorption features (Figure 10). The ATREM corrected images expressed the lowest change over
394   time for the VNIR and IR, as described by the trend values (close to zero) and lowest CV.   Overall,

395 the CV was < 5% across the spectrum, except in bands adjacent to atmospheric absorption regions.
396 No significant (p < 0.01) or rapid degradation was apparent for any spectral interval during the
397 precession period for the three correction approaches. The quadrature values were similar for the
398 entire dataset (Quadratures 2004-2016) as well as for the last five years of the mission (Quadratures
399 2011-2016).   We found that locations having terrain slopes greater than 15° introduced a peak
400 value in anomaly trends as compared to dune flats of 0 to 10°.   Trends progressively increased for
401 slopes up to 15°, then oscillated 2 to 5% in the VIS and > 20% in the SWIR, due to Hyperion imaging
402 both the illuminated and shaded portions of dunes. The BRDF information about large dunes in the
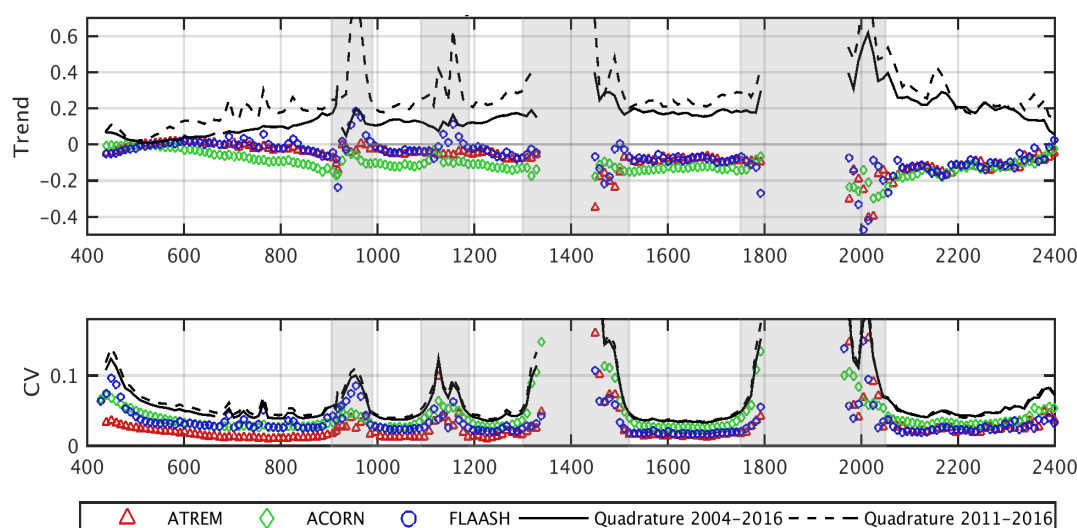403 Libya-4 PICS is important for cross-calibrating Earth observing sensors.
404

Figure 10. Means of 172 calibrated Hyperion bands from 36 images acquired from 2004 to 2016 after use of 3 atmospheric correction models: (top row) least squares fit linear trend in surface reflectance; (bottom row) coefficient of variation (CV). The quadrature (combined uncertainty) is calculated as the square root of the sum of squares. Gray areas indicate atmospheric absorption bands [52].

4. Discussion

411   The catalyst for this study was EO-1's declining orbit and this work evaluated how it affected
412 its instrument's data quality and stability though time. In general, we demonstrate that surface
413 reflectance retrievals were not seriously affected during the late mission precession period, typically
414 being within 5% for VIS and 10% longer wavelengths for most surfaces, although the Libya-4 PICS
415 desert variation was slightly higher due mostly, we suspect, to large dunes casting larger shadows
416 from increased SZA from earlier overpass times. Other land cover types, including croplands and
417 deciduous forests, were shown to have differences in reflectance between dates, but showed
418 consistency when looking at their derivatives. All land cover types that we looked at, however, did
419 not show marked increase or decrease in NDVI over the full precession range of our time series. It
420 should also be stated that we avoided high off-nadir sensor view angles when selecting our images
421 to minimize variance due to view geometry differences.
422   The effect of precession on other sensors has been studied and we can compare our results to
423 theirs. Swinnen, et al.[22] measured orbital drift and its effects on Satellite Pour l'Observation de la
424 Terre (SPOT) data, finding somewhat similar or slightly higher differences in spectral reflectance
425 that ranged from 10% - 20% when in reference to another sensor, but the impact on NDVI was
426 negligible.   We assume that the reason their study obtained slightly higher variances than ours
427 was because the two SPOT sensors that were compared (i.e., VGT1 and VGT2) had differences in
428 calibration accuracies, as well as slightly different spectral response functions
429   This work provides insight on the limits of increasing SZAs on EO-1 surface reflectance data
430 quality. This issue is important not only for the creation of consistent long-term satellite time series,

431 but also help to define issues in combining data from multiple satellites with different overpass
432 times, as have been proposed for future satellite constellations, and to merge existing or past data
433 collections. Atmospheric correction models account for differences in the measured upwelling
434 radiance for different acquisition dates and times and results could differ if only TOA products are
435 used. Future work could study the limits of even earlier crossing times to see at what point the
436 increased SZA starts to negatively affect data quality. Hagolle [53] found that the relative difference
437 in reflectance values and NDVI increased moderately with increase in initial SZA up to 50°, but
438 beyond this, an increase in SZA resulted in an exponential change in relative difference. While
439 this result is important, it was based on simulated SPOT data and only evaluated four multispectral
440 bands. Our study is current as of late-2016, when the minimum SZA reached 50° (see Fig. 3).
441 Early in 2017, the last images were collected and the mission was decommissioned. At this point the
442 minimum SZA was around 55°, preventing us from determining the effects on data as the sun
443 approaches the horizon at overpass time.

444 Nevertheless, the first space-based measurements of a large methane leak from the Aliso
445 Canyon, California super emitter were captured by Hyperion in January 2016 under low winter sun
446 angles, and later verified by aircraft observations, demonstrating that even a nearly invisible gas
447 plume above a complex landscape could be detected from orbit with a spectrometer [54]. This
448 opens new possibilities for future monitoring capabilities if NASA chooses to support a mission
449 similar to the one identified by the National Research Council in the 2007 Decadal Survey for Earth
450 Sciences, which defined a Pre-Phase-A mission, the Hyperspectral InfraRed Imager (HyspIRI).

451 **5. Conclusions**

452 In this study, multispectral and hyperspectral remote sensing imagery were evaluated from
453 the EO-1's two spectral imagers, ALI and Hyperion, in comparison with data from the Landsat and
454 MODIS sensors. Our analyses were done at a mid-latitude mixed forest site, two desert PIC sites, a
455 USDA agricultural research site, and a northern experimental forest. ALI NDVI was compared to
456 Landsat NDVI, Hyperion reflectance was examined before and during orbital precession using
457 time-series for Hyperion NDVI data compared to MODIS NDVI and using spectral derivative
458 analyses. Additionally, we evaluated the role that different atmospheric correction algorithms had
459 on time-series Hyperon imagery. We have shown in this study that the sensors onboard the EO-1
460 satellite have produced robust products for scientific analysis of the Earth during its entire 16 year
461 mission. This study took a multi-faceted approach to quantify EO-1 data quality and we
462 determined that no marked decline exists for either ALI or Hyperion when compared with other
463 highly calibrated and stable sensors in a diverse set of locations. The variability is typically within
464 5% for the VNIR and within 10% for the SWIR wavelengths, excluding bands near atmospheric
465 absorption features, which is in the range of previous EO-1 data quality estimates that were made
466 before the satellite's orbit started precession [3,12]. Lastly, it was found that this variability in
467 retrieved surface reflectance is not seriously affected among three commonly employed
468 atmospheric correction techniques. This is encouraging for time-series analysis, when it is often
469 pertinent to correct for differing atmospheric conditions that may be present.

470 It is important to note that these results are current as of mid-2016. Median overpass times will
471 continue to get earlier and greater solar zenith angles will be experienced. In October 2016 the
472 overpass time reached 8AM local time and the satellite started the decommission protocol, which
473 will be completed in March 2017. In between that time users should be cautious when using EO-1
474 data as data quality under these circumstances has not been evaluated.

479 **Author Contributions**: Shannon Franks was the primary author and all other authors contributed
480 to writing the final paper. Elizabeth Middleton, EO-1 mission scientist, organized the

481 implementation of the studies. Shannon Franks coordinated the work and also did the "Park Falls
482 EO-1 ALI NDVI vs. Landsat NDVI" study, Petya Campbell performed the "RRVP PICS" study,
483 Guoqing Sun performed the "BARC Derivative Analysis" study, Qingyuan Zhang and Tian Yao
484 performed the "Howland NDVI comparison to MODIS NDVI" study, Christopher Neigh
485 performed the "Libya-4 PICS" study, Karl Huemmrich provided the figures on orbital precession,
486 and Steve Ungar provided information on orbital precession and historical mission context**.**

487 **Conflicts of Interest:** The authors declare no conflict of interest.

488 **Abbreviations**

489 The following abbreviations are used in this manuscript:
490
491 ACORN: Atmospheric CORrection Now
492 ALI: Advanced Land Imager
493 ATREM: Atmosphere Removal
494 BARC: Beltsville Agricultural Research Center
495 BRDF: Bi-Directional Reflectance Distribution Function
496 CEOS: Committee on Earth Observing Satellites
497 CV: Coefficient of Variation
498 EO-1: Earth Observing One
499 ETM+: Enhanced Thematic Mapper plus
500 FLAASH: Fast Line-of-sight Atmospheric Analysis of Spectral Hypercubes
501 TM: Thematic Mapper
502 MODIS: Moderate Resolution Imaging Spectroradiometer
503 NDVI: Normalized Difference Vegetation Index
504 NIR: Near Infrared
505 PICS: Pseudo-Invariant Calibration Site
506 RRVP: Rail Road Valley Playa
507 SNR: Signal to Noise Ratio
508 SWIR: Short Wave Infrared
509 SZA: Solar Zenith Angle
510 TOA: Top of Atmosphere
511 USGS: United States Geological Survey
512 VNIR: Visible Near Infrared
513 WRS: Worldwide Reference System
514

515 **References**

516 1.   Elmore, A.J.; Mustard, J.F. Precision and Accuracy of EO-1 Advanced Land Imager (ALI)
517   Data for Semiarid Vegetation Studies. *Ieee Transactions on Geoscience and Remote Sensing*
518   **2003**, *41*, 1311-1320.
519 2.   Datt, B.; McVicar, T.R.; Van Niel, T.G.; Jupp, D.L.B.; Pearlman, J.S. Preprocessing EO-1
520   Hyperion Hyperspectral Data to Support the Application of Agricultural Indexes. *Ieee*
521   *Transactions on Geoscience and Remote Sensing* **2003**, *41*, 1246-1259.
522 3.   Ungar, S.G.; Pearlman, J.S.; Mendenhall, J.A.; Reuter, D. Overview of the Earth Observing
523   One (EO-1) Mission. *Ieee Transactions on Geoscience and Remote Sensing* **2003**, *41*, 1149-1159.
524 4.   Bryant, R.; Moran, M.S.; McElroy, S.A.; Holifield, C.; Thome, K.J.; Miura, T.; Biggar, S.F.
525   Data Continuity of Earth Observing 1 (EO-1) Advanced Land Imager (ALI) and Landsat
526   Tm and ETM. *Ieee Transactions on Geoscience and Remote Sensing* **2003**, *41*, 1204-1214.

527 5. Pu, R.; Yu, Q.; Gong, P.; Biging, G.S. EO-1 Hyperion, ALI and Landsat 7 ETM+ Data
528 Comparison for Estimating Forest Crown Closure and Leaf Area Index. *International Journal*
529 *of Remote Sensing* **2005**, *26*, 457-474.

530 6. Roy, D.P.; Wulder, M.A.; Loveland, T.R.; Woodcock, C.E.; Allen, R.G.; Anderson, M.C.;
531 Helder, D.; Irons, J.R.; Johnson, D.M.; Kennedy, R.; Scambos, T.; Schaaf, C.B.; Schott, J.R.;
532 Sheng, Y.; Vermote, E.F.; Belward, A.S.; Bindschadler, R.; Cohen, W.B.; Gao, F.; Hipple, J.D.;
533 Hostert, P.; Huntington, J.; Justice, C.O.; Kilic, A.; Kovalskyy, V.; Lee, Z.P.; Lymbumer, L.;
534 Masek, J.G.; McCorkel, J.; Shuai, Y.; Trezza, R.; Vogelmann, J.; Wynne, R.H.; Zhu, Z.
535 Landsat-8: Science and Product Vision for Terrestrial Global Change Research. *Remote*
536 *Sensing of Environment* **2014**, *145*, 154-172.

537 7. Irons, J.R.; Dwyer, J.L.; Barsi, J.A. The Next Landsat Satellite: The Landsat Data Continuity
538 Mission. *Remote Sensing of Environment* **2012**, *122*, 11-21.

539 8. Ungar, S. Personal Communication. **12/27/2016**.

540 9. Middleton, E.M.; Ungar, S.G.; Mandl, D.J.; Ong, L.; Frye, S.W.; Campbell, P.E.; Landis, D.R.;
541 Young, J.P.; Pollack, N.H. The Earth Observing One (EO-1) Satellite Mission: Over a Decade
542 in Space. *Ieee Journal of Selected Topics in Applied Earth Observations and Remote Sensing* **2013**,
543 *6*, 243-256.

544 10. Fagan, M.E.; DeFries, R.S.; Sesnie, S.E.; Arroyo-Mora, J.P.; Soto, C.; Singh, A.; Townsend,
545 P.A.; Chazdon, R.L. Mapping Species Composition of Forests and Tree Plantations in
546 Northeastern Costa Rica with an Integration of Hyperspectral and Multitemporal Landsat
547 Imagery. *Remote Sensing* **2015**, *7*, 5660-5696.

548 11. White, J.C.; Gomez, C.; Wulder, M.A.; Coops, N.C. Characterizing Temperate Forest
549 Structural and Spectral Diversity with Hyperion EO-1 Data. *Remote Sensing of Environment*
550 **2010**, *114*, 1576-1589.

551 12. Blanco, P.D.; del Valle, H.F.; Bouza, P.J.; Metternicht, G.I.; Hardtke, L.A. Ecological Site
552 Classification of Semiarid Rangelands: Synergistic Use of Landsat and Hyperion Imagery.
553 *Int J Appl Earth Obs* **2014**, *29*, 11-21.

554 13. Chen, S.; Fang, L.; Li, H.; Chen, W.; Huang, W. Evaluation of a Three-Band Model for
555 Estimating Chlorophyll-a Concentration in Tidal Reaches of the Pearl River Estuary, China.
556 *ISPRS-J. Photogramm. Remote Sens.* **2011**, *66*, 356-364.

557 14. Chen, S., ; Fang, L; Li, H.; Chen, W.; Huang, W. Evaluation of a Three-Band Model for
558 Estimating Chlorophyll-a Concentration in Tidal Reaches of the Pearl River Estuary, China.
559 *ISPRS Journal of Photogrammetry and Remote Sensing* **2011**, *66*, 356-364.

560 15. Brando, V.E.; Dekker, A.G. Satellite Hyperspectral Remote Sensing for Estimating Estuarine
561 and Coastal Water Quality. *Ieee Transactions on Geoscience and Remote Sensing* **2003**, *41*,
562 1378-1387.

563 16. Chudnovsky, A.; Kostinski, A.; Herrmann, L.; Koren, I.; Nutesku, G.; Ben-Dor, E.
564 Hyperspectral Spaceborne Imaging of Dust-Laden Flows: Anatomy of Saharan Dust Storm
565 from the Bodele Depression. *Remote Sensing of Environment* **2011**, *115*, 1013-1024.

566 17. Chien, S.; Doubleday, J.; Mclaren, D.; Tran, D.; Tanpipat, V.; Chitradon, R.;
567 Boonya-aroonnet, S.; Thanapakpawin, P.; Mandl, D. Monitoring Flooding in Thailand
568 Using Earth Observing One in a Sensorweb. *Ieee Journal of Selected Topics in Applied Earth*
569 *Observations and Remote Sensing* **2013**, *6*, 291-297.

18. Davies, A.G.; Chien, S.; Doubleday, J.; Tran, D.; Thordarson, T.; Gudmundsson, M.T.; Hoskuldsson, A.; Jakobsdottir, S.S.; Wright, R.; Mandl, D. Observing Iceland's Eyjafjallajokull 2010 Eruptions with the Autonomous Nasa Volcano Sensor Web. *J Geophys Res-Sol Ea* **2013**, *118*, 1936-1956.

19. Mandl, D.; Frye, S.; Cappelaere, P.; Handy, M.; Policelli, F.; Katjizeu, M.; Van Langenhove, G.; Aube, G.; Saulnier, J.F.; Sohlberg, R.; Silva, J.A.; Kussul, N.; Skakun, S.; Ungar, S.G.; Grossman, R.; Szarzynski, J. Use of the Earth Observing One (EO-1) Satellite for the Namibia Sensorweb Flood Early Warning Pilot. *Ieee Journal of Selected Topics in Applied Earth Observations and Remote Sensing* **2013**, *6*, 298-308.

20. Davies, A.G.; Chien, S.; Baker, V.; Doggett, T.; Dohm, J.; Greeley, R.; Ip, F.; Castano, R.; Cichy, B.; Rabideau, G.; Tran, D.; Sherwood, R. Monitoring Active Volcanism with the Autonomous Sciencecraft Experiment on EO-1. *Remote Sensing of Environment* **2006**, *101*, 427-446.

21. Ramsey, M.S.; Flynn, L.P. Strategies, Insights, and the Recent Advances in Volcanic Monitoring and Mapping with Data from Nasxs Earth Observing System. *J Volcanol Geoth Res* **2004**, *135*, 1-11.

22. Swinnen, E.; Verbeiren, S.; Deronde, B.; Henry, P. Assessment of the Impact of the Orbital Drift of SPOT-VGT1 by Comparison with SPOT-VGT2 Data. *International Journal of Remote Sensing* **2014**, *35*, 2421-2439.

23. Devasthale, A.; Grassl, H. Dependence of Frequency of Convective Cloud Occurrence on the Orbital Drift of Satellites. *International Journal of Remote Sensing* **2007**, *28*, 3701-3706.

24. Negri, A.J.; Bell, T.L.; Xu, L.M. Sampling of the Diurnal Cycle of Precipitation Using Trmm. *J Atmos Ocean Tech* **2002**, *19*, 1333-1344.

25. USGS EROS. Available Online: www.Earthexplorer.Com (Accessed on 24 August 2016).

26. Rouse, J.W.; Haas, R.H.; Schell, J.A.; Deering, D.W. Monitoring Vegetation Systems in the Great Plains with Erts. *NASA Special Publication 351* **1974**.

27. Tucker, C.J. Red and Photographic Infrared Linear Combinations for Monitoring Vegetation. *Remote Sensing of Environment* **1979**, *8*, 127-150.

28. Galvao, L.S.; Ponzoni, F.J.; Epiphanio, J.C.N.; Rudorff, B.F.T.; Formaggio, A.R. Sun and View Angle Effects on Ndvi Determination of Land Cover Types in the Brazilian Amazon Region with Hyperspectral Data. *International Journal of Remote Sensing* **2004**, *25*, 1861-1879.

29. Homer, C.; Dewitz, J.; Yang, L.M.; Jin, S.; Danielson, P.; Xian, G.; Coulston, J.; Herold, N.; Wickham, J.; Megown, K. Completion of the 2011 National Land Cover Database for the Conterminous United States - Representing a Decade of Land Cover Change Information. *Photogrammetric Engineering and Remote Sensing* **2015**, *81*, 345-354.

30. Gao, B.C.; Davis, C.O. Development of a Line-by-Line-Based Atmosphere Removal Algorithm for Airborne and Spaceborne Imaging Spectrometers. *P Soc Photo-Opt Ins* **1997**, *3118*, 132-141.

31. Gao, B.C.; Heidebrecht, K.B.; Goetz, A.F.H. Derivation of Scaled Surface Reflectances from Aviris Data. *Remote Sensing of Environment* **1993**, *44*, 165-178.

32. NASA. Level-1 and Atmosphere Archive & Distribution System (Laads). **https://ladsweb.nascom.nasa.gov/ (last accessed 12/30/2016)**.

612   33.   Zhang, Q.Y.; Cheng, Y.B.; Lyapustin, A.I.; Wang, Y.J.; Gao, F.; Suyker, A.; Verma, S.;
613   Middleton, E.M. Estimation of Crop Gross Primary Production (GPP): fAPAR(Chl) Versus
614   MOD15A2 FPAR. *Remote Sensing of Environment* **2014**, *153*, 1-6.

615   34.   Lyapustin, A.I.; Wang, Y.J.; Laszlo, I.; Hilker, T.; Hall, F.G.; Sellers, P.J.; Tucker, C.J.; Korkin,
616   S.V. Multi-Angle Implementation of Atmospheric Correction for MODIS (MAIAC): 3.
617   Atmospheric Correction. *Remote Sensing of Environment* **2012**, *127*, 385-393.

618   35.   Felde, G.W.; Anderson, G.P.; Cooley, T.W.; Mathew, M.W.; adler-Golden, S.M.; Berk, A.;
619   Lee, J. In *Analysis of Hyperion Data with the FLAASH Atmospheric Correction Algorithm*,
620   Geoscience and Remote Sensing Symposium. IGARSS '03, 21-25 July 2003, 2003; 2003 IEEE
621   International: pp 90-92.

622   36.   Tsai, F.; Philpot, W. Derivative Analysis of Hyperspectral Data. *Remote Sensing of
623   Environment* **1998**, *66*, 41-51.

624   37.   Kalluri, H.R.; Prasad, S.; Bruce, L.M. Decision-Level Fusion of Spectral Reflectance and
625   Derivative Information for Robust Hyperspectral Land Cover Classification. *Ieee
626   Transactions on Geoscience and Remote Sensing* **2010**, *48*, 4047-4058.

627   38.   Ye, Z.; He, M.Y.; Fowler, J.E.; Du, Q. Hyperspectral Image Classification Based on Spectra
628   Derivative Features and Locality Preserving Analysis. *2014 Ieee China Summit &
629   International Conference on Signal and Information Processing (Chinasip)* **2014**, 138-142.

630   39.   Cleveland, W.S. Robust Locally Weighted Regression and Smoothing Scatterplots. *J Am Stat
631   Assoc* **1979**, *74*, 829-836.

632   40.   Exelis Visual Information Solutions, B., Colorado.

633   41.   Teillet, P.M.; Barsi, J.A.; Chander, G.; Thome, K.J.; Xiong, J. Prime Candidate Earth Targets
634   for the Post-Launch Radiometric Calibration of Space-Based Optical Imaging Instruments.
635   *Proceedings of SPIE* **2007**, *6677*, 66770S-66770S-66712.

636   42.   Scott K.P., T.K.J., Brownlee M.R. Evaluation of the Railroad Valley Playa for Use in
637   Vicarious Calibration. *Proc. of SPIE* **1996**, *2818*, 158-166.

638   43.   Teillet, P.M.; Ren, X.M. In *Spectral Band Difference Effects on Vegetation Indices Derived from
639   Multiple Satellite Sensor Data*, Canadian Journal of Remote Sensing, Jun, 2008; pp 159-173.

640   44.   Czapla-Myers, J.S.; Thome, K.J.; Biggar, S.F. Design, Calibration, and Characterization of a
641   Field Radiometer Using Light-Emitting Diodes as Detectors. *Applied Optics* **2008**, *47*,
642   6753-6762.

643   45.   Czapla-Myers, J.; Ong, L.; Thome, K.; McCorkel, J. Validation of EO-1 Hyperion and
644   Advanced Land Imager Using the Radiometric Calibration Test Site at Railroad Valley,
645   Nevada. *Ieee Journal of Selected Topics in Applied Earth Observations and Remote Sensing* **2016**,
646   *9*, 816-826.

647   46.   Campbell, P.K.E.; Middleton, E.M.; Thome, K.J.; Kokaly, R.F.; Huemmrich, K.F.;
648   Lagomasino, D.; Novick, K.A.; Brunsell, N.A. EO-1 Hyperion Reflectance Time Series at
649   Calibration and Validation Sites: Stability and Sensitivity to Seasonal Dynamics. *Ieee Journal
650   of Selected Topics in Applied Earth Observations and Remote Sensing* **2013**, *6*, 276-290.

651   47.   (AIG). ACORN User's Guide, Stand Alone Version. *Analytical Imaging and Geophysics LLC*
652   **2001**, 64.

653   48.   Kruse, F.A.; Boardman, J.W.; Huntington, J.F. Comparison of Airborne Hyperspectral Data
654   and EO-1 Hyperion for Mineral Mapping. *Ieee T Geosci Remote* **2003**, *41*, 1388-1400.

655 49. Gao, B.C.; Goetz, A.F.H. Column Atmospheric Water Vapor and Vegetation Liquid Water
656 Retrievals from Airborne Imaging Spectrometer Data. *Journal of Geophysical Research* **1990**,
657 *95*, 3549-3564.

658 50. Kruse, F.A. In *Comparison of ATREM, ACORN, and FLAASH Atmospheric Corrections Using*
659 *Low-Altitude AVIRIS Data of Boulder, Colorado*, 13th JPL Airborne Geoscience Workshop, Jet
660 Propulsion Laboratory March 31 - April 2 2004, 2004; Jet Propulsion Laboratory pp 1-10.

661 51. Taylor, J.R. *An Introduction to Error Analysis the Study of Uncertainties in Physical*
662 *Measurements*. University Science Books: United States of America, 1939; p 327.

663 52. Neigh, C.S.R.; McCorkel, J.; Campbell, P.; Ong, L.; Ly, V.; Landis, D.; Fry, S.; Middleton,
664 E.M. Monitoring Orbital Precession of EO-1 Hyperion with Three Atmospheric Correction
665 Models in the Libya-4 Pics. *IEEE Geoscience and Remote Sensing Letters* **2016**, *12*, 1797-1801.

666 53. Hagolle, O. Effet D'un Changement D'Heure De Passage Sur Les Séries Temporelles De
667 Données De L'Instrument Vegetation. *Toulouse: CNES* **2007**, *6*.

668 54. Thompson, D.R.; Thorpe, A.K.; Frankenberg, C.; Green, R.O.; Duren, R.; Guanter, L.;
669 Hollstein, A.; Middleton, E.; Ong, L.; Ungar, S. Space-Based Remote Imaging Spectroscopy
670 of the Aliso Canyon CH4 Superemitter. *Geophysical Research Letters* **2016**, *43*, 6571–6578.